

Research Paper

Inversion method of deflection of the vertical based on SWOT wide-swath altimeter data



Xin Liu ^{a,*}, Menghao Song ^a, Chao Li ^b, Guihua Hui ^a, Jinyun Guo ^a, Yongjun Jia ^c,
Heping Sun ^d

^a College of Geodesy and Geomatics, Shandong University of Science and Technology, Qingdao 266590, China

^b Weicheng Branch of Natural Resources and Planning Bureau of Weifang City, Weifang 261021, China

^c National Satellite Ocean Application Service, Beijing 100081, China

^d State Key Laboratory of Geodesy and Earth's Dynamics, Innovation Academy for Precision Measurement Science and Technology, Chinese Academy of Science, Wuhan 420071, China

ARTICLE INFO

Article history:

Received 24 May 2023

Accepted 11 November 2023

Available online 16 December 2023

Keywords:

SWOT

Wide-swath altimeter

Inversion method of DOV

Multi-directional

Arabian sea

ABSTRACT

The deflection of the vertical (DOV) is the key information in the study of ocean gravity field. However, in most areas, the precision of the prime component of DOV is significantly lower than that of the meridian component. To obtain higher accuracy and resolution of ocean gravity information, researchers have proposed a novel altimeter called the wide-swath altimeter. This altimeter allows for the simultaneous acquisition of high-precision and high-resolution two-dimensional measurements of sea surface height (SSH). In this paper, the Surface Water and Ocean Topography (SWOT) mission with a wide-swath altimeter on board is selected for research. One cycle of SWOT sea surface height data is simulated to inverse the DOV in the Arabian Sea (45°E–80°E, 0°–30°N), and the inversion results are compared with those of conventional altimeter data. The results demonstrate that the difference between the meridian and prime components derived from the inversion of SWOT wide-swath data is minimal, significantly outperforming the inversion results of conventional nadir altimeter data. The advantage of SWOT wide-swath altimeter lies in its ability to use the multi-directional geoid slope at any sea surface measurement point to invert the components in the meridian and prime directions. To investigate the impact of this advantage on inversion precision, this paper employs a method to calculate the gradient of the geoid in multiple directions to invert DOV components. The improvement effect of calculating the gradient of the geoid in multiple directions on the precision of DOV component is analyzed. It is found that the accuracy of DOV inversion has significantly improved with the increase of geodetic gradient calculation direction. In addition, the effects of various errors and grid spacing in SWOT wide sea surface height data on the precision of DOV inversion are also analyzed.

© 2023 Editorial office of Geodesy and Geodynamics. Publishing services by Elsevier B.V. on behalf of KeAi Communications Co. Ltd. This is an open access article under the CC BY-NC-ND license (<http://creativecommons.org/licenses/by-nc-nd/4.0/>).

* Corresponding author.

E-mail address: xinliu1969@126.com (X. Liu).

Peer review under responsibility of Institute of Seismology, China Earthquake Administration.



Production and Hosting by Elsevier on behalf of KeAi

1. Introduction

Satellite altimetry is the main technique for obtaining ocean gravity information [1]. Since the inception of the first altimetry mission over 50 years ago, the quantity and quality of satellite altimetry data products have improved significantly [2–4]. Calculating the deflection of the vertical (DOV) is a common method for obtaining ocean gravity information. Traditional DOV measurement methods are susceptible to natural factors such as waves and tides. The progress of satellite altimetry technology has effectively alleviated the limitations of conventional methods [5,6]. Consequently, there has been a continuous enhancement in both the precision

and resolution of DOV inversion. Nevertheless, due to the lack of synchronous sea surface height (SSH) measurements in the vertical direction of orbit, most conventional nadir altimeters can only calculate the along-track DOV, unable to determine the cross-track DOV [7–9].

With the application of Ka-band radar altimeter and synthetic aperture radar (SAR) altimeter [10], wide-swath altimeters have been proposed as novel altimeters that can recover higher precision and resolution of ocean gravity field information. Space exploration agencies, including the National Aeronautics and Space Administration, the French Centre National d'Études Spatiales, the United Kingdom Space Agency, and the Canadian Space Agency, have collaboratively developed the Surface Water and Ocean Topography (SWOT) altimeter mission [11]. The primary hydrological objective of SWOT mission is to acquire high-resolution measurements of global terrestrial water heights, alterations in water reserves, and stream flows [12,13]. When applied to oceanography, it enables high-resolution global SSH measurements and the detection of ocean eddies at sub-mesoscale [14–16].

SWOT mission operates on a repeating cycle of approximately 21 days, with a total mission duration of 3.5 years. The satellite carries various payloads, including a Ka-band radar interferometer (KaRIn), a traditional altimeter similar to Jason-2/Poseidon pulse-limited dual-frequency (Ku and C-band), and a three-frequency microwave radiometer similar to Jason-2/ARM [17]. Additionally, precise orbit/positioning systems are incorporated into the satellite. Among these payloads, KaRIn holds significant importance as one of the key payloads of the SWOT satellite. Its capability of distinguishing ocean signals surpasses that of conventional nadir altimeters by an order of magnitude [11]. Furthermore, KaRIn enables the acquisition of high-precision and high-resolution wide-swath interferometric measurement data of water surface and ocean. It provides two-dimensional grid SSH data with a grid spacing of no more than 2 km. Using interferometry technology in SWOT enhances the accuracy of SSH measurements and effectively mitigates noise [18].

In this study, we first invert DOV components using one cycle of SWOT simulation data and one-year simulation observation data from three conventional nadir altimeters, namely, Jason-1/GM (Geodetic Mission), CryoSat-2/LRM (Low-Resolution Mode) and SARAL/GM. Through comparison, it is verified that inverting DOV component with SWOT wide-swath data can significantly improve the precision of the prime DOV component. To fully harness the characteristics and advantages of SWOT wide-swath altimeter data [19], the multi-directional geoid gradients at any grid sea surface point are calculated when inverting the meridian and prime components of DOV, and the improvement effect of this calculation method on inversion precision is analyzed in this paper. Furthermore, various errors that may be present in SWOT data, particularly those induced by Ka-band radar interferometers, are simulated and analyzed. We quantify the impact of various errors on the precision of DOV and apply filtering to enhance the inversion precision. In the subsequent section, we investigate the impact of the grid spacing of SWOT sea surface height measurement data on the precision of DOV inversion. This analysis aims to offer guidance for future efforts in constructing high-precision and high-resolution ocean gravity field models using SWOT wide-swath altimeter data [20].

2. Experimental data

The Arabian Sea area (45°E–80°E, 0°–30°N) is situated at the convergence of the Asia-Europe Plate, the Indian Ocean Plate, and the African Plate, featuring active geological processes and intricate seafloor topography. The reason for selecting this area for research is that it can effectively demonstrate the advantages of applying

SWOT data to the inversion of DOV and gravity anomaly. The Arabian Sea area is taken as an example to simulate a 21-day cycle of SWOT sea surface height data for subsequent processing and analysis in this research. The dataset comprises two wide swaths of two-dimensional grid data with a width of 50 km, along with the nadir ground tracks. The interval between the two wide swaths is 20 km, and the distance from the nadir ground tracks to any swath is 10 km. Two sets of data with different grid spacing (1 km × 1 km and 2 km × 2 km) are simulated to research the impact of grid spacing on the accuracy of DOV.

To simulate SWOT wide-swath data, a two-dimensional longitude and latitude grid is recovered using satellite ground track files, and then SSH is interpolated on the grid [21]. We interpolate the mean sea surface (MSS) model and the daily delayed-time sea level anomaly (SLA) product onto a wide swath grid to generate simulated SSH observations. The MSS model selects MSS_CNES_2015 [22] from AVISO, and the SLA product comes from the European Copernicus Program [23]. To eliminate the influence of mean dynamic topography (MDT) on SSH, the simulated SSH values are corrected by subtracting the MDT_CNES_CLS18 [24] model obtained from AVISO.

According to the error budget document [19], the measurement error on the SWOT wide swath includes instrument error and geophysical correction model error. The instrument error, caused by instruments carried by SWOT, mainly includes KaRIn error, roll error, phase error, baseline dilation error, and timing error. Regarding geophysical correction model error, this study focuses on evaluating the impact of wet troposphere delay error on precision. Other geophysical correction model errors, such as those related to the dry troposphere and ionosphere, are not considered due to their smaller magnitudes [25].

The effect of roll error (δ_{roll}) on the SSH at any sea point P can be mathematically represented as follows [19]:

$$\delta h = C \left(1 + \frac{H}{R_E} \right) \delta_{\text{roll}} \quad (1)$$

where C represents the distance from the specific point P to the nadir track, and R_E corresponds to the radius of the Earth (about 6371 km). Additionally, H denotes the ellipsoidal height of the SWOT interferometer antenna. Eq. (1) reveals a linear relationship, indicating that the impact of roll error on the observed SSH at point P increases proportionally with the distance from the nadir track towards the swath edge.

The SSH error induced by phase error (δ_{phase}) can be expressed as follows [19]:

$$\delta h = \frac{C}{k_B} \left(1 + \frac{H}{R_E} \right) \delta_{\text{phase}} \quad (2)$$

where k is the reciprocal of the electromagnetic wavelength, i.e., the electromagnetic wavenumber and B is the baseline length, which is the distance (10 m) between the two interferometer antennas of the SWOT satellite. Similar to roll error, phase error also exhibits a linear increase across the entire swath.

Baseline dilation error (δ_{dilation}) is caused by variations in baseline length, and its effect on SSH can be mathematically expressed as follows [19]:

$$\delta h = - \left(1 + \frac{H}{R_E} \right) \frac{C^2}{H_B} \delta_{\text{dilation}} \quad (3)$$

where it can be observed that the error in SSH due to baseline dilation error is proportional to the square of the distance between the sea surface point P and the nadir of the satellite.

The effect of timing error (δ_{timing}) on SSH is expressed as follows [19]:

$$\delta h = \frac{c}{2} \cos \theta \delta_{\text{timing}} \quad (4)$$

where c is the speed of light, and θ is the viewing angle. For points with the same θ , the time error has the same impact.

The height error resulting from KaRIn error varies according to the grid spacing of SSH data and the distance from the nadir of SSH data. In addition, it is also affected by effective wave height [19]. To simulate KaRIn error, a constant value of 2 m is employed to represent the significant wave height, as depicted in Fig. 1(e).

Wet tropospheric delay correction error is the residual error that still exists after wet tropospheric delay corrected by the microwave radiometer on SWOT satellite [18].

Based on the ground track file of SWOT satellite [11,19], a total of 584 data products are generated in one cycle for global measurements, comprising data products of 292 ascending tracks and 292 descending tracks. Using the data product with track number 501 as an example, Fig. 1 illustrates the varying errors and the total error present in SWOT wide swath.

Fig. 1 reveals that only Ka-band radar interferometer error demonstrates randomness among the six simulated errors, while the other five errors exhibit systematic characteristics. Except for KaRIn error, the phase error has the highest numerical value. As depicted in Eq. (2) and Fig. 1(a), it is evident that its magnitude

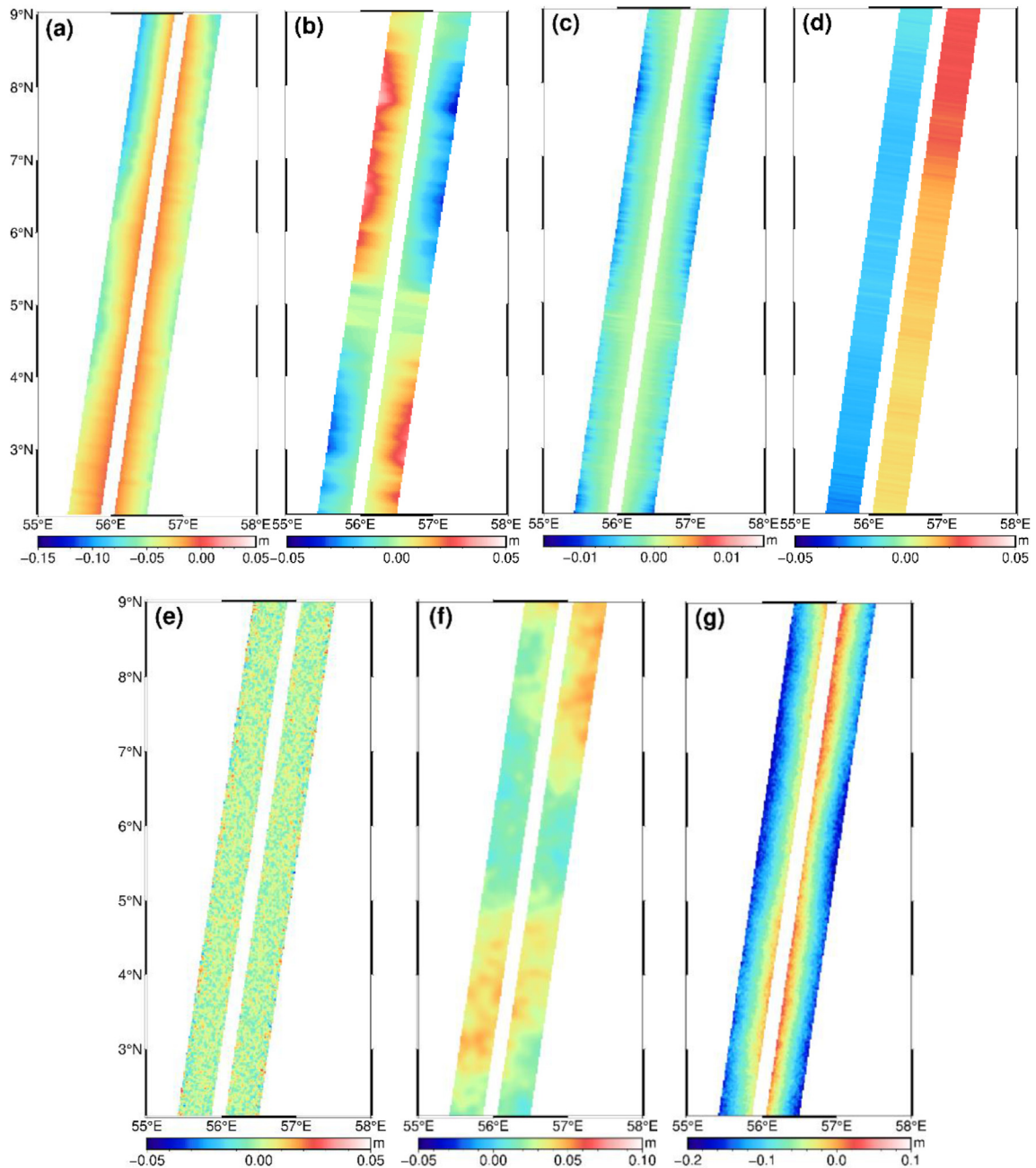


Fig. 1. Errors included in the swath of SWOT simulation measurements: (a) phase error; (b) roll error; (c) baseline dilation error; (d) timing error; (e) Ka-band radar interferometer error (KaRIn error); (f) wet tropospheric delay correction error; and (g) total error.

increases as the distance from the ground track grows. The roll error displays a left-right mirrored distribution on both sides of the ground track, while the baseline dilation error exhibits a symmetrical distribution with respect to the nadir ground track. The timing error remains independent on both the left and right swaths. The magnitudes of the various errors are approximately equal, with the baseline dilation error being the smallest [26].

The primary objective of this study is to investigate the SWOT wide-swath grid data. Compared with the conventional nadir altimeter employed by SWOT, the wide-swath altimeter collects a considerably larger volume of data. As a result, simulated altimetry data from the conventional nadir altimeter carried by SWOT are not utilized in the experiment. In addition, the selection of MSS and MDT models has a limited impact on the analysis [21]. To minimize potential errors in the comparison, the same SLA data and MSS model are employed to simulate SSH data for the conventional nadir altimeters, namely Jason-1/GM, CryoSat-2/LRM and SARAL/GM. Subsequently, these simulated data are compared with the inverted results of DOV obtained using SWOT wide-swath data. For the simulated SWOT sea surface height data, the grid spacing and the nadir spacing are set to 2 km. Furthermore, the SSH simulation data from three traditional altimeters are resampled along the orbit at a 2 km sampling interval.

3. Methodology

Based on the above information, we generate simulated SSH data for the SWOT wide-swath altimeter through MSS and SLA interpolation. This SSH dataset comprises both geoid height and MDT. We subtract MDT from the simulated SWOT wide-swath SSH data to derive SWOT geoid height. Subsequently, we remove the geoid height from the EGM2008 model [27] to obtain the residual geoid height. We utilize the residual geoid heights N_Q and N_P at N and P of two adjacent sea surface observation points on the SWOT grid, along with the specified distance dist_{PQ} between them, to compute residual DOV ε_{PQ} and the residual geoid gradient e_{PQ} [28] as follows:

$$\varepsilon_{PQ} = -e_{PQ} = \frac{N_Q - N_P}{\text{dist}_{PQ}} \quad (5)$$

Due to the orbital spacing, conventional nadir altimeter data can only be used to calculate the along-track DOV. This implies that the geoid gradient in one direction is calculated for the inversion of DOV component (as illustrated in Fig. 2(a)). Consequently, as the orbital inclination of conventional nadir altimeters increases, the precision of the meridian component gradually improves while the precision of the prime component gradually decreases, resulting in noticeable differences in the precision of these two components. To fully leverage the benefits of wide swath grid data, SWOT sea surface height data are used to compute the multi-directional geoid gradients (Fig. 2(b)) around any grid sea surface point for the inversion of DOV components. Section 4.2 explores the impact of calculating the multi-directional geoid gradients to retrieve DOV on accuracy.

After obtaining the residual geoid height, we employ the least squares collocation method to obtain residual DOV components on the grid [28] as follows:

$$\begin{pmatrix} \xi_{\text{res}} \\ \eta_{\text{res}} \end{pmatrix} = \begin{pmatrix} \mathbf{C}_{\xi e} \\ \mathbf{C}_{\eta e} \end{pmatrix} (\mathbf{C}_{ee} + \mathbf{C}_n)^{-1} \mathbf{e}_{\text{res}} \quad (6)$$

where ξ_{res} and η_{res} represent the meridian component and prime component of residual DOV at the point; $\mathbf{C}_{\xi e}$ is the covariance matrix of the residual geoid gradient of the meridian component

residual DOV; $\mathbf{C}_{\eta e}$ is the covariance matrix of the residual geoid gradient of the prime component residual DOV; \mathbf{C}_{ee} is the variance-covariance matrix of the residual geoid gradient; \mathbf{C}_n is the geoid gradient noise variance matrix; and \mathbf{e}_{res} is the residual gradient of the geoid.

The radial component \mathbf{l} and transverse component \mathbf{m} of the geoid gradient are related to DOV components as follows:

$$\begin{cases} \mathbf{l} = \xi \cos \alpha_{PQ} + \eta \sin \alpha_{PQ} \\ \mathbf{m} = \eta \cos \alpha_{PQ} - \xi \sin \alpha_{PQ} \end{cases} \quad (7)$$

where α_{PQ} is the azimuth of P to Q .

The relationship between the geoid components and DOV components at the grid point P to be solved can be obtained by Eq. (8):

$$\begin{cases} \xi = \mathbf{l} \cos \alpha_{PQ} - \mathbf{m} \sin \alpha_{PQ} \\ \eta = \mathbf{l} \sin \alpha_{PQ} + \mathbf{m} \cos \alpha_{PQ} \end{cases} \quad (8)$$

The geoid gradient of P and Q point can be expressed by the corresponding radial and transverse components of the geoid gradient as follows:

$$\begin{cases} \mathbf{e}_P = \mathbf{l}_P \cos(\alpha_{e_P} - \alpha_{PQ}) + \mathbf{m}_P \sin(\alpha_{e_P} - \alpha_{PQ}) \\ \mathbf{e}_Q = -\mathbf{l}_Q \cos(\alpha_{e_Q} - \alpha_{QP}) - \mathbf{m}_Q \sin(\alpha_{e_Q} - \alpha_{QP}) \end{cases} \quad (9)$$

where the gradient of geoid at point P is recorded as \mathbf{e}_P , the radial component is \mathbf{l}_P , the transverse component is \mathbf{m}_P ; the gradient of geoid at point Q is recorded as \mathbf{e}_Q , the radial component is \mathbf{l}_Q , the transverse component is \mathbf{m}_Q ; the orbital inclination of the satellite at point P is denoted as α_{e_P} , and denoted as α_{e_Q} at point Q ; α_{PQ} and α_{QP} represent the orbital inclination from P to Q and that from Q to P .

Thus, the covariance between the geoid component and the geoid gradient at the grid point P can be obtained:

$$\begin{aligned} \text{cov}(\xi_P, \mathbf{e}_Q) &= -\text{cov}(\mathbf{l}_P, \mathbf{l}_Q) \cos \alpha_{PQ} \cos(\alpha_{e_Q} - \alpha_{QP}) \\ &\quad + \text{cov}(\mathbf{m}_P, \mathbf{m}_Q) \sin \alpha_{PQ} \sin(\alpha_{e_Q} - \alpha_{QP}) \end{aligned} \quad (10)$$

$$\begin{aligned} \text{cov}(\eta_P, \mathbf{e}_Q) &= -\text{cov}(\mathbf{l}_P, \mathbf{l}_Q) \sin \alpha_{PQ} \cos(\alpha_{e_Q} - \alpha_{QP}) \\ &\quad - \text{cov}(\mathbf{m}_P, \mathbf{m}_Q) \cos \alpha_{PQ} \sin(\alpha_{e_Q} - \alpha_{QP}) \end{aligned} \quad (11)$$

Therefore, the covariance between residual DOV and the residual geoid gradient is derived from Ref. [29]:

$$\begin{cases} \mathbf{C}_{\xi e} = -\mathbf{C}_{ll} \cos \alpha_{PQ} \cos(\alpha_{e_Q} - \alpha_{QP}) + \mathbf{C}_{mm} \sin \alpha_{PQ} \sin(\alpha_{e_Q} - \alpha_{QP}) \\ \mathbf{C}_{\eta e} = -\mathbf{C}_{ll} \sin \alpha_{PQ} \cos(\alpha_{e_Q} - \alpha_{QP}) - \mathbf{C}_{mm} \cos \alpha_{PQ} \sin(\alpha_{e_Q} - \alpha_{QP}) \end{cases} \quad (12)$$

Using Eq. (6), residual DOV at the grid point is calculated. Then, the DOV of the reference gravity field is recovered and the DOV at the grid point is obtained.

4. Results and discussion

4.1. Comparison between SWOT wide-swath altimeter and traditional altimeter inversion of DOV

A comparative experiment is conducted using a 21-day cycle of SWOT simulated data and 1-year simulated data from Jason-1/GM, CryoSat-2/LRM and SARAL/GM. Additionally, a combined dataset from the three conventional nadir altimeters is used (simulated by the method described in Section 2). To ensure the result accuracy, residual DOV components with a 2' grid spacing in both the meridional and prime directions are calculated for comparison.

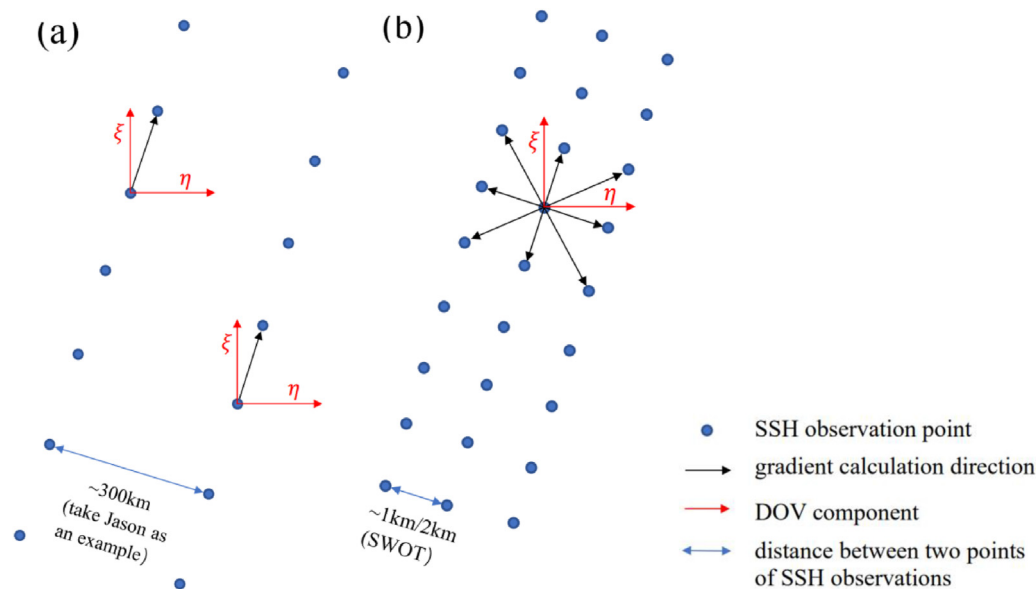


Fig. 2. DOV calculation diagram of (a) conventional nadir altimeters data (taking Jason series satellites as an example) and (b) SWOT wide-swath altimeter data (taking the calculation of DOV in 8 directions as an example).

This is done because a 1-year duration of conventional nadir altimeter data may not provide sufficient information for inverting DOV components with a 1' grid spacing [21]. Table 1 presents the statistical results of residual DOV components. In this study, SWOT wide-swath altimeter data are used to invert DOV components by computing the deflection in eight directions.

Table 1 demonstrates that compared to the EGM2008 model, the meridian and prime components computed from SWOT data exhibit the least deviation, signifying superior inversion results compared to the three conventional nadir altimeters and the combined datasets. The relative precision of the inverted DOV component using just one cycle of SWOT data can achieve a level comparable to that of traditional satellites with a year's worth of data in the meridian direction, and a significant enhancement is exhibited in the prime direction. For instance, the difference is reduced by almost 50 % (0.176'' compared to 0.091'') when compared with the result from the Jason-1/GM dataset. The inversion results of the Jason-1/GM dataset have the slightest difference between the two components in the three conventional altimeter datasets. This validates the efficacy of SWOT wide-swath altimeter data in reducing the disparity between the meridian and prime components.

When conventional nadir altimeters invert DOV component, they can only utilize the geoid gradient in one direction for calculation. With an increase in satellite orbital inclination (66° for Jason-1, 88°/92° for CryoSat-2 and 81.5°/98.5° for SARAL), the precision of the meridian component in conventional nadir

altimeters improves, but the precision of the prime DOV decreases. This results in a noticeable increase in the disparity between the meridian and prime components. Conversely, when inverting the deflection components using SWOT wide-swath altimeter data, the precision of the prime vertical direction is enhanced by calculating the geoid gradient in multiple directions. This leads to a substantial reduction in the precision gap between the meridian and prime components.

4.2. Inversion of DOV by calculating multi-directional geoid gradient

Compared with conventional nadir altimeters, SWOT wide-swath altimeter data enjoys a unique advantage. It efficiently utilizes multi-directional geoid gradients to invert the meridian and prime components. This characteristic significantly enhances inversion precision, which is unavailable to conventional nadir altimeters. To assess the impact of multi-directional geoid slope gradients on the precision of meridional and prime components, three distinct sets of experiments are conducted. The KaRIn error contained in SWOT data varies with grid spacing, and the inversion results of SWOT sea surface height data with a 1 km grid spacing are more affected by errors than those with a 2 km grid spacing. To highlight the effect of errors, we use SWOT data with a grid spacing of 1 km for experiments. The influence of grid spacing on the precision of the DOV component inversion is discussed in Section 4.5.

Fig. 3 shows the three experimental groups, and Experiment 1 (hereafter abbreviated as Exp.1 in Table 2) employed simulation data of error-free SSH and data containing all SSH errors to invert residual DOV components in the meridian and prime directions. This is done by calculating the 4-direction residual geoid gradient at a sea surface point. In Experiment 2 and Experiment 3, the residual geoid gradients in 8 and 16 directions are calculated, respectively.

The inversion results of error-free SSH data are used as the reference object for three sets of experiments. Table 2 shows the differences between the DOV components of the inversions of the three SSH datasets containing errors and the inversion results of the error-free data.

Table 1
Comparison of residual DOV components obtained from SWOT and traditional altimeter data (unit: arcsec).

Dataset	Meridian component				Prime component			
	Min	Max	Mean	STD	Min	Max	Mean	STD
SWOT	−8.14	8.46	−0.01	0.34	−8.52	8.60	0.01	0.44
Jason-1/GM	−9.99	5.48	0.01	0.34	−8.53	10.08	−0.02	0.52
CryoSat-2/LRM	−7.01	7.82	−0.03	0.30	−7.90	8.72	−0.12	0.87
SARAL/GM	−9.01	7.61	−0.01	0.30	−9.51	9.90	−0.01	0.65
Combined dataset	−8.21	7.82	0.02	0.39	−7.90	8.91	−0.02	0.84

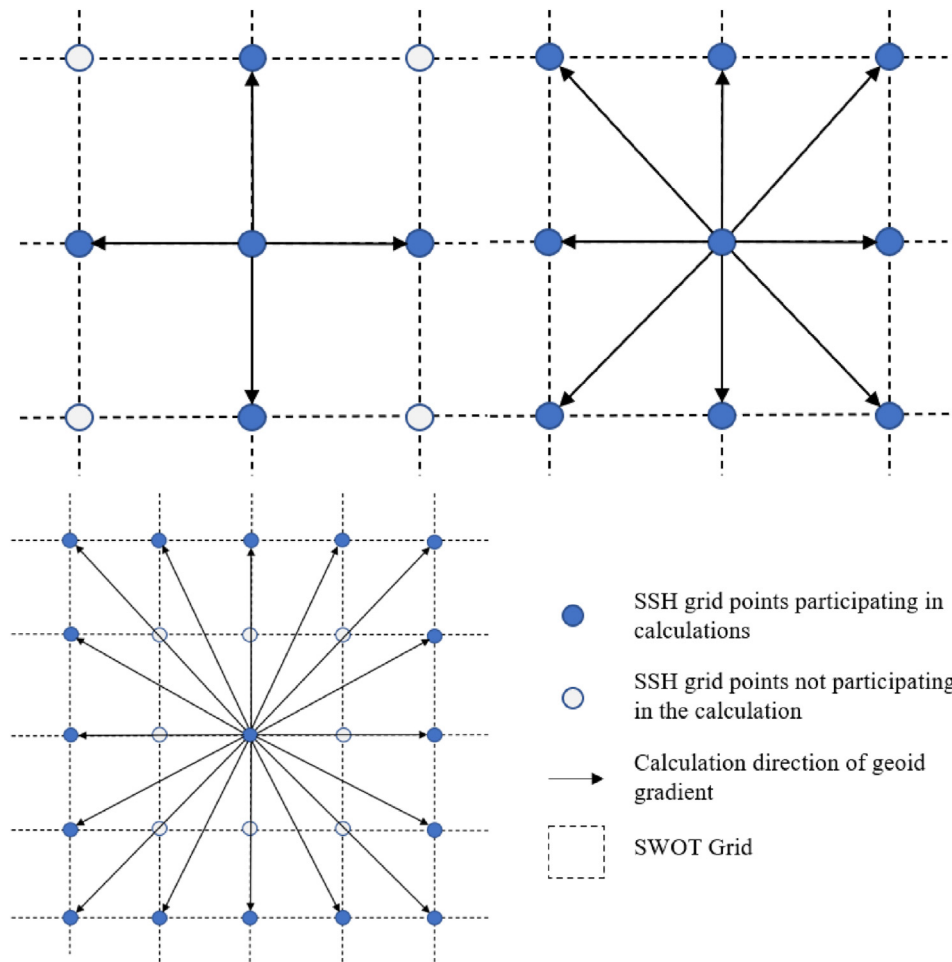


Fig. 3. Schematic diagram for computing multi-directional (4, 8, 16) geoid gradients at any sea surface grid point.

Table 2

Statistics of DOV components calculated by multi-directional geoid gradients (unit: arcsec).

Component	Experience	Min	Max	Mean	STD	RMSE
Meridian	Exp.1	−13.78	16.81	−0.01	2.04	2.04
	Exp.2	−12.57	14.62	−0.01	1.66	1.66
	Exp.3	−9.44	9.86	−0.01	1.23	1.23
Prime	Exp.1	−17.14	17.63	0.02	1.99	1.99
	Exp.2	−16.67	13.17	0.02	1.57	1.57
	Exp.3	−7.69	8.74	0.02	1.12	1.12

Table 2 illustrates that with an increase in the number of calculation directions, the impact of errors on the meridian and prime components diminishes significantly. As the number of calculation directions increases from 4 to 16, the precision of both the meridian and prime components converges towards the inversion result of error-free data. The discrepancy is minimal between the precision of the DOV components obtained through geoid gradient inversion in 16 directions and that of the error-free data inversion result. The disparity between the calculation results of the meridian and prime components STD and the error-free data can reach 1.23" and 1.12", respectively. Compared to the calculation using a 4-direction geoid gradient, the difference between the inversion result and the error-free data inversion result is reduced by approximately 0.8".

The comparison of the three sets of experiments clearly illustrates that when using SWOT data to invert the DOV component, the

increase in the number of calculation directions for the geoid significantly enhances inversion precision. This underscores the principal rationale for the advantages of SWOT wide-swath altimeter data over conventional nadir altimeters in DOV calculations for recovering marine gravity field models. Nonetheless, augmenting the number of calculation directions for the geoid surface gradient will substantially raise computational demands, potentially diminishing efficiency. In future research, while considering the hardware computational performance, increasing the number of calculation directions for the gradient of the geoid surface can be adopted to reduce the impact of various errors on the precision of DOV component. The goal is to construct a higher-precision and higher-resolution ocean DOV and gravity field models while ensuring efficiency.

4.3. Effect of errors on DOV

According to the SWOT error budget document [19], KaRIn error differs from other system errors and exhibits a random distribution within the grid (Fig. 1(e)). Consequently, it significantly affects the inversion of DOV. Phase error, roll error, and baseline dilation error exert a moderate influence, whereas timing error and residual wet troposphere error have less impact. The effect of roll error, phase error, and baseline dilation error on the calculation of DOV cannot be eliminated since they are influenced by the distance from the nadir. Although timing error remains consistent along the orbit direction and can be removed, it introduces errors when estimating gradients in other directions. Moreover, the residual wet troposphere error

cannot be eliminated and does not exhibit a discernible correlation with the distance from the nadir. To mitigate the effect of KaRIn error on precision of DOV, filtering techniques can be adopted [30,31].

The effect of KaRIn error on DOV changes with grid spacing. Upon comparing residual DOV derived from SWOT data at 1 km and 2 km grid spacing, it is observed that residual DOV calculated with 1 km grid spacing is more susceptible to KaRIn error than that with 2 km grid spacing. In Section 4.2, it has been discovered that the calculation of the multi-directional geoid gradients can reduce the impact of the error on component precision when inverting DOV component. Therefore, to highlight the error and showcase the advantages of SWOT data in calculating multi-directional geoid gradients, we use SWOT sea surface height data with 1 km grid spacing to calculate 8-direction geoid gradients and obtain the meridian and prime components of 1' grid DOV. The effect of SSH grid spacing on DOV will be discussed in subsequent sections.

To quantify the impact of each error on precision of DOV inversion, we select the meridian and prime DOV components obtained from the error-free SWOT sea surface height data as a reference and compare them with corresponding components calculated from SWOT sea surface height data containing individual error and total error. Here, we perform experiments by calculating 8-direction geodetic gradients at a single sea surface point to invert DOV components. The statistical results in Table 3 illustrate that these errors significantly compromise the precision of residual DOV inversion, with a particularly significant impact of KaRIn error.

Previous studies [32] have extensively examined the effects of orbit error, geophysical errors and tide effect. In this study, we focus on analyzing and comparing the effects of six types of errors (Table 4). Compared to KaRIn error, phase error and roll error have a relatively minor impact; however, they exhibit a more pronounced influence on the meridian component than on the prime component. The impact of roll error is approximately half that of phase error, but it still exerts a more pronounced influence on the precision of the meridian component than on the prime component. Conversely, the impact of baseline dilation error on precision of DOV is relatively minor, and the same holds true for timing error and wet tropospheric delay correction error.

4.4. Effect of filter on DOV

Previous researches have shown that filtering techniques can effectively reduce KaRIn error [30,31]. In this study, we employ a two-dimensional Gaussian filter to mitigate the impact of KaRIn

Table 4

Comparison statistics of filtering effects of Gaussian filter with different filtering radius (unit: arcsec).

Component	Filter radius (km)	Min	Max	Mean	STD	RMSE
Meridian	Unfiltered	−12.57	14.62	−0.01	1.66	1.66
	5	−14.49	15.00	−0.03	0.57	0.57
	10	−14.78	16.05	−0.02	0.56	0.56
	15	−15.12	16.07	−0.02	0.57	0.57
Prime	Unfiltered	−16.67	13.17	0.02	1.57	1.57
	5	−13.12	12.95	0.01	0.32	0.32
	10	−21.62	14.10	0.01	0.30	0.30
	15	−15.43	20.84	0.01	0.31	0.31

error on precision [21]. Considering that SWOT data are different from traditional satellite-observed SSH data, a suitable filter radius should be selected. In the case of SWOT data with a 1 km grid spacing for SSH, we conduct experiments using three distinct Gaussian filters with radius of 5 km, 10 km, and 15 km, all of which calculate the geoid gradient in 8 directions to invert DOV components. DOV components, computed from error-free SWOT data, serve as a reference to assess filtering effectiveness.

Table 4 illustrates the results of three sets of experiments, which exhibit minimal variations. However, compared with 5 km and 15 km filters, the Gaussian filter with a 10 km radius demonstrates superior effectiveness in filtering SWOT sea surface height data. After filtering, the precision of residual DOV components in the meridian and prime directions, calculated from SSH data in 8 directions of the geoid, has improved compared with unfiltered data. Specifically, the difference between filtered data and error-free data has decreased from 1.66" to 1.57"—0.56" and 0.30" for the meridian and prime components, respectively.

The difference in precision between the two components after filtering is possible because the Gaussian filter mainly filters KaRIn error. In contrast, its effectiveness on systematic errors with regularity, such as phase and rolling errors in the swath, is relatively limited. As is shown in Table 3, other errors, especially phase and rolling errors, have a greater effect on the precision of the meridian component than that of the prime component. This research confirms that employing a two-dimensional Gaussian filter effectively mitigates KaRIn error, nearly eradicating their impact on the precision of DOV calculations following filtration. This once again proves that KaRIn errors are the largest source of error.

4.5. Effect of SSH grid spacing on DOV

To evaluate the impact of SWOT data with different grid spacings on the precision of DOV inversion, we conduct simulations of SWOT sea surface height data with grid spacings of 1 km × 1 km and 2 km × 2 km. The calculation of 8-directional geoid gradients is performed to invert residual DOV components with a resolution of 1'.

Higher-resolution SSH data can recover higher-resolution ocean gravity field models with guaranteed precision. However, as the grid spacing decreases, the precision of SSH decreases as well. To address this concern, increasing the grid spacing and applying filtering techniques can effectively reduce errors and enhance the precision [33]. Here, we conduct experiments using SSH data containing errors and SSH data filtered for errors. Considering that this section intends to explore the comparative influence of SWOT data with varying grid spacings on the precision of DOV components, we employ a consistent 10 km Gaussian filter radius to process the data. Table 5 presents the results using the inversion results obtained from error-free SSH data as a reference.

Table 5 illustrates the influence of varying grid spacing on the meridian and prime components of DOV. With an increase in grid

Table 3

Statistics of the effect of errors on residual DOV (unit: arcsec).

Errors	Meridian component				
	Min	Max	Mean	STD	RMSE
Phase	−1.91	2.59	−0.03	0.42	0.42
Roll	−0.96	0.85	−0.01	0.19	0.19
Dilation	−0.41	0.59	−0.01	0.04	0.04
Timing	−0.42	1.30	−0.01	0.02	0.02
KaRIn	−12.27	12.84	−0.02	1.54	1.54
Troposphere	−0.48	0.29	−0.01	0.06	0.06
Total	−12.57	14.62	−0.01	1.66	1.66
Errors	Prime component				
	Min	Max	Mean	STD	RMSE
Phase	−2.28	0.98	0.01	0.09	0.09
Roll	−0.61	0.49	0.01	0.05	0.05
Dilation	−0.60	4.10	0.01	0.07	0.07
Timing	−3.62	4.08	0.01	0.09	0.09
KaRIn	−10.75	11.69	0.01	1.49	1.49
Troposphere	−0.42	0.30	0.01	0.06	0.06
Total	−16.67	13.17	0.02	1.57	1.57

Table 5
Statistical results of DOV component inverted from SWOT data with different grid spacings (unit: arcsec).

Component	Experience	Min	Max	Mean	STD	RMSE
Meridian	With error/1 km	−12.57	14.62	−0.01	1.66	1.66
	With error filtered/1 km	−14.78	16.05	−0.02	0.56	0.56
	With error/2 km	−5.93	5.88	0.01	0.71	0.71
Prime	With error filtered/2 km	−15.33	20.14	−0.02	0.55	0.55
	With error/1 km	−16.67	13.17	0.02	1.57	1.57
	With error filtered/1 km	−21.62	14.10	0.01	0.30	0.30
	With error/2 km	−4.97	4.51	0.02	0.61	0.61
	With error filtered/2 km	−12.64	20.31	0.01	0.27	0.27

spacing from 1 km to 2 km, the impact of various errors on the precision of DOV components is significantly mitigated. Filtering is conducted using a two-dimensional Gaussian filter with a radius of 10 km. After filtering, the 2D impact of the error on the precision of two SWOT SSH datasets with different grid spacing is significantly reduced. The experiment reveals that, despite higher errors in SSH data with a 1 km grid spacing, filtered data can still be utilized to calculate high-precision DOV components. Hence, if the errors in 1 km SSH data can be further mitigated to enhance accuracy, SWOT data may be employed to recover high-precision/high-resolution ocean gravity field models with a grid spacing of less than 1' [21].

5. Conclusion

As a novel altimeter, the wide-swath altimeter provides considerably higher resolution for SSH measurements compared with conventional nadir altimeters. With the SWOT altimetry mission as an example, its onboard wide-swath altimeter has the capability to generate wide-swath SSH data. This data can be employed to derive high-precision and high-resolution DOV components, effectively addressing issues arising from distinct disparities between the meridian and prime components caused by factors such as the satellite orbit inclination.

Based on SWOT information and documents currently known [19], one cycle of SWOT wide-swath altimeter data is simulated in the Arabian Sea area, and a related study is conducted to evaluate its application in DOV calculation. Compared with conventional nadir altimeters, which can only calculate the along-track geoid gradients to invert DOV components, SWOT wide-swath altimeter data can use geoid gradients in multiple directions to invert DOV components, significantly reducing the difference between the meridian and prime components. To verify this feature and the advantage of SWOT wide swath altimeter data, this study calculates the geodetic gradients in four, eight, and sixteen directions to invert DOV components. It is revealed that, as the number of calculation directions increases, the impact of errors is notably diminished, resulting in a substantial improvement in precision. Moreover, the precision of the meridian and prime components closely approaches the inversion results of error-free data. Considering computational efficiency in future studies, the impact of the errors on the precision of DOV components can be reduced by increasing the computational direction of geoid gradients, thereby constructing the ocean DOV and gravity field models with higher precision and resolution.

Despite various errors in SWOT data, KaRIn error has the greatest impact on inversion results, which can be mitigated by filtering. Other significant errors include phase error, roll error, and baseline dilation error. To examine the impact of different grid

spacing on the precision of DOV components, experiments have been conducted using SWOT data with a grid spacing of 1 km and 2 km. The results indicate that the DOV components obtained from the 2 km grid spacing SWOT data are less affected by errors and have higher precision compared to the 1 km grid spacing data. However, through filtering, DOV components with equivalent precision can also be obtained using the 1 km grid spacing data. It provides the possibility for constructing DOV and gravity field models with a grid spacing of less than 1' in the future.

In future research, to enhance the precision and resolution of DOV and gravity field models, mitigating the influence of errors on DOV components can be achieved by expanding the computational directions of the geoid gradient while considering computational efficiency. However, unresolved issues include dealing with the persistent diamond-shaped grid gaps after multiple cycles of SWOT altimeter and addressing the wide swath intersections. It is necessary to tackle these challenges in further research.

Author contributions

Conceptualization: X.L. and M.S.; methodology: X.L., M.S. and J.G.; software: M.S. and G.H.; validation: M.S. and G.H.; formal analysis: X.L. and C.L.; investigation: C.L., Y.J.; resources: J.G.; data curation: X.L. and M.S.; writing-original draft preparation: M.S.; writing-review and editing: X.L., J.G.; visualization: C.L. and G.H.; supervision: J.G. and H.-S.; project administration: X.L. and J.G.; funding acquisition: J.G. All authors have read and agreed to the published version of the manuscript.

Declaration of competing interest

Heping Sun is the Editor-in-Chief and Jinyun Guo is an Editorial Board Member for Geodesy and Geodynamics. They were not involved in the editorial review or the decision to publish this article. All authors declare that there are no competing interests.

Acknowledgments

The SWOT simulator is provided by Jet Power Laboratory, accessed at https://github.com/CNES/swot_simulator. Additionally, the nadir ground tracks and other related information of SWOT can be obtained from AVISO (<https://www.aviso.altimetry.fr/en/data/products/sea-surface-height-products/global/simulated-swot-products.html>). We express our sincere gratitude to these institutions and websites for their valuable contributions.

This research has received financial support from the National Natural Science Foundation of China (No. 42274006, 42192535, 42242015).

References

[1] D.T. Sandwell, H. Harper, B. Tozer, W.H.F. Smith, Gravity field recovery from geodetic altimeter missions, *Adv. Space Res.* 68 (2) (2021) 1059–1072, <https://doi.org/10.1016/j.asr.2019.09.011>.
[2] C. Hwang, E.T. Chang, Geophysics. Seafloor secrets revealed, *Science* 346 (6205) (2014) 32–33, <https://doi.org/10.1126/science.1260459>.
[3] D. Sandwell, D. Müller, W. Smith, E. Garcia, R. Francis, New global marine gravity from CryoSat-2 and Jason-1 reveals buried tectonic structure, *Science* 346 (2014) 65–67, <https://doi.org/10.1126/science.1258213>.
[4] H. Ji, X. Liu, C.-C. Zhu, J.-J. Yuan, B. Ji, J.Y. Guo, On performance of CryoSat-2 altimeter data in deriving marine gravity over the Bay of Bengal, *Mar. Geophys. Res.* 42 (4) (2021) 39, <https://doi.org/10.1007/s11001-021-09461-x>.
[5] J.Y. Guo, X. Liu, Y.N. Chen, J.B. Wang, C.M. Li, Local normal height connection across sea with ship-borne gravimetry and GNSS techniques, *Mar. Geophys. Res.* 35 (2) (2014) 141–148, <https://doi.org/10.1007/s11001-014-9216-x>.

- [6] R.K. Raney, L. Phalippou, The future of coastal altimetry, in: S. Vignudelli, Cipollini P. KostianoyAG, J. Benveniste (Eds.), *Coastal altimetry*, Springer, Berlin, 2011, pp. 535–560.
- [7] J.Y. Guo, Y. Shen, K.H. Zhang, X. Liu, Q.L. Kong, F. Xie, Temporal-spatial distribution of oceanic vertical deflections determined by TOPEX/Poseidon and Jason-1/2 missions, *Earth Sci. Res. J.* 20 (2016) 1–5, <https://doi.org/10.15446/esrj.v20n2.54402>.
- [8] H. Ji, J.Y. Guo, C.-C. Zhu, J.-J. Yuan, X. Liu, G. Li, On deflections of vertical determined from HY-2A/GM altimetry data in the bay of bengal, *IEEE J. Sel. Top. Appl. Earth Obs. Rem. Sens.* 14 (2021) 12048–12060, <https://doi.org/10.1109/JSTARS.2021.3129273>.
- [9] X. Liu, G.H. Hui, J.Y. Guo, T.H. Zhang, M.H. Song, Inversion of deflection of the vertical in the south China sea using ICESat-2 sea surface height data, *Rem. Sens.* 15 (1) (2023) 30, <https://doi.org/10.3390/rs15010030>.
- [10] S.J. Zhang, D. Sandwell, Retracking of SARAL/AltiKa radar altimetry waveforms for optimal gravity field recovery, *Mar. Geodesy* 40 (1) (2017) 40–56, <https://doi.org/10.1080/01490419.2016.1265032>.
- [11] S. Desai, L. Fu, S. Cherali, P. Vaze, *Surface water and Ocean Topography mission (SWOT) project science requirements document*, in: Technical report JPL D-61923, Jet propulsion laboratory, National Aeronautics and Space Administration, Pasadena, 2018.
- [12] H. Lee, M. Durand, H.C. Jung, D. Alsdorf, C.K. Shum, Y. Sheng, Characterization of surface water storage changes in Arctic lakes using simulated SWOT measurements, *Int. J. Rem. Sens.* 31 (14) (2010) 3931–3953, <https://doi.org/10.1080/01431161.2010.483494>.
- [13] E.H. Altenau, T.M. Pavelsky, M.T. Durand, X. Yang, R.P.d.M. Frasson, L. Bendezu, The surface water and Ocean Topography (SWOT) mission river database (sword): a global river network for satellite data products, *Water Resour. Res.* 57 (7) (2021), <https://doi.org/10.1029/2021WR030054> e2021WR030054.
- [14] S. Biancamaria, K.M. Andreadis, M. Durand, E.A. Clark, E. Rodriguez, N.M. Mognard, D.E. Alsdorf, D.P. Lettenmaier, Y. Oudin, Preliminary characterization of SWOT hydrology error budget and global capabilities, *IEEE J. Sel. Top. Appl. Earth Obs. Rem. Sens.* 3 (1) (2010) 6–19, <https://doi.org/10.1109/JSTARS.2009.2034614>.
- [15] R.D. Müller, K.J. Matthews, D.T. Sandwell, Advances in imaging small-scale seafloor and sub-seafloor tectonic fabric using satellite altimetry, first ed., CRC Press, Boca Raton, 2017 <https://doi.org/10.1201/9781315151779-16>.
- [16] A. Chaudhary, N. Agarwal, R. Sharma, S.P. Ojha, R. Kumar, Nadir altimetry Vis-à-Vis swath altimetry: a study in the context of SWOT mission for the Bay of Bengal, *Rem. Sens. Environ.* 252 (2021) 112120, <https://doi.org/10.1016/j.rse.2020.112120>.
- [17] Z. Li, X. Liu, J.Y. Guo, C.-C. Zhu, J.-J. Yuan, J.Y. Gao, Y.G. Gao, B. Ji, Performance of Jason-2/GM altimeter in deriving marine gravity with the waveform derivative retracking method: a case study in the South China Sea, *Arabian J. Geosci.* 13 (18) (2020) 939, <https://doi.org/10.1007/s12517-020-05960-0>.
- [18] C. Uebmann, L.-L. Fu, S. Brown, E. Peral, D. Esteban-Fernandez, The effect of atmospheric water vapor content on the performance of future wide-swath ocean altimetry measurement, *Journal of Atmospheric and Oceanic Technique* 31 (6) (2014) 1446–1454, <https://doi.org/10.1175/JTECH-D-13-00179.1>.
- [19] D. Esteban-Fernandez, L.-L. Fu, B. Pollard, Swot project: Mission performance and error budget, Technical Report JPL D-79084, in: Jet propulsion laboratory, National Aeronautics and Space Administration, Pasadena, 2017.
- [20] G. Louis, M.-F. Lequentrec-Lalancette, J.-Y. Royer, D. Rouxel, L. Géli, M. Maïa, M. Faillot, Ocean gravity models from future satellite missions, *Eos, Transactions American Geophysical Union* 91 (3) (2010) 21–22, <https://doi.org/10.1029/2010EO030001>.
- [21] T.Y. Jin, M. Z. H. Zhang, J.C. Li, W.P. Jiang, S.J. Zhang, M.Z. Hu, Analysis of vertical deflections determined from one cycle of simulated SWOT wide-swath altimeter data, *J. Geodesy* 96 (4) (2022) 30, <https://doi.org/10.1007/s00190-022-01619-8>.
- [22] P. Schaeffer, I. Pujol, Y. Faugere, The CNES CLS 2015 global mean sea surface, Presentation OSTST, 2016. La Rochelle, https://www.avisio.altimetry.fr/gallery/entry_221_mean_sea_surface_2015.html.
- [23] G. Taburet, A. Sanchez-Roman, M. Ballarotta, M.I. Pujol, J.F. Legeais, F. Fournier, Y. Faugere, G. Dibarboure, Duacs DT2018: 25 years of reprocessed sea level altimetry products, *Ocean Sci.* 15 (5) (2019) 1207–1224, <https://doi.org/10.5194/os-15-1207-2019>.
- [24] S. Mulet, M.H. Rio, H. Etienne, C. Artana, M. Cancet, G. Dibarboure, H. Feng, R. Husson, N. Picot, C. Provost, P.T. Strub, The new CNES-CLS18 global mean dynamic topography, *Ocean Sci.* 17 (3) (2021) 789–808, <https://doi.org/10.5194/os-17-789-2021>.
- [25] D.C. Yu, C. Hwang, O.B. Andersen, E.T.Y. Chang, L. Gaultier, Gravity recovery from SWOT altimetry using geoid height and geoid gradient, *Rem. Sens. Environ.* 265 (2021) 112650, <https://doi.org/10.1016/j.rse.2021.112650>.
- [26] L. Gaultier, C. Uebmann, L.-L. Fu, The challenge of using future SWOT data for oceanic field reconstruction, *Journal of Atmospheric and Oceanic Technique* 33 (1) (2016) 119–126, <https://doi.org/10.1175/JTECH-D-15-0160.1>.
- [27] N.K. Pavlis, S.A. Holmes, S.C. Kenyon, J.K. Factor, The development and evaluation of the Earth gravitational model 2008 (EGM2008), *J. Geophys. Res. Solid Earth* 117 (2012) B04406, <https://doi.org/10.1029/2011JB008916>.
- [28] C.-C. Zhu, J.Y. Guo, J.Y. Gao, X. Liu, C. Hwang, S.W. Yu, J.-J. Yuan, B. Ji, B. Guan, Marine gravity determined from multi-satellite GM/ERM altimeter data over the South China Sea: SCSGA V1.0, *J. Geodesy* 94 (5) (2020) 50, <https://doi.org/10.1007/s00190-020-01378-4>.
- [29] C. Hwang, B. Parsons, Gravity anomalies derived from Seasat, Geosat, ERS-1 and TOPEX/POSEIDON altimetry and ship gravity: a case study over the Reykjanes Ridge, *Geophys. J. Int.* 122 (2) (1995) 551–568, <https://doi.org/10.1111/j.1365-246X.1995.tb07013.x>.
- [30] L. Gómez-Navarro, R. Fablet, E. Mason, A. Pascual, B. Mourre, E. Cosme, J. Le Sommer, SWOT spatial scales in the western mediterranean sea derived from pseudo-observations and an ad hoc filtering, *Rem. Sens.* 10 (4) (2018) 599, <https://doi.org/10.3390/rs10040599>.
- [31] L. Gómez-Navarro, E. Cosme, J.L. Sommer, N. Papadakis, A. Pascual, Development of an image de-noising method in preparation for the surface water and Ocean Topography satellite mission, *Rem. Sens.* 12 (4) (2020) 734, <https://doi.org/10.3390/rs12040734>.
- [32] S.J. Zhang, J.C. Li, T.Y. Jin, D.F. Che, Assessment of radar altimetry correction slopes for marine gravity recovery: a case study of Jason-1GM data, *J. Appl. Geophys.* 151 (2018) 90–102, <https://doi.org/10.1016/j.jappgeo.2018.02.003>.
- [33] L.-L. Fu, E. Rodriguez, Towards mapping the ocean surface topography at 1 km resolution, 2006. <https://hdl.handle.net/hdl:2014/39826>.



Xin Liu received her Ph.D. degree from Shandong University of Science and Technology in 2007. Now she is an associate professor in College of Geodesy and Geomatics of Shandong University of Science and Technology, Qingdao, China. Her research interests include spatial data processing and data mining.



Menghao Song is pursuing his master's degree at Shandong University of Science and Technology. His research direction is space geodesy.



Chao Li now is an engineer of Weicheng Branch of Natural Resources and Planning Bureau of Weifang City, Weifang, China. His research interests include surveying engineering and remote sensing.



Guihua Hui received her master's degree from Shandong University of Science and Technology in 2023. Her research direction is space geodesy.



Yongjun Jia received the B.S. degree in information and computing science from Inner Mongolia University, Hohhot, China, and the M.S. and Ph.D. degrees in physical oceanography from the Institute of Oceanology, Chinese Academy of Sciences, Qingdao, China, in 2007 and 2010, respectively. He is currently a Researcher with National Satellite Ocean Application Service, Beijing, China. His research interests include ocean microwave remote sensing and satellite oceanography.



Jinyun Guo obtained his Ph.D. degree in Geodesy and Surveying Engineering from the Shandong University of Science and Technology, in 2004. He is currently a professor at College of Geodesy and Geomatics, Shandong University of Science and Technology, Qingdao, China. His current research interests include space geodesy and geophysics.



Heping Sun was born in Jiangsu, China, in 1955. He received the B.S. degree from the University of Science and Technology of China, Hefei, China, in 1980, and obtained Ph.D. degree from Catholic University of Louvain, Belgium, in 1995. He is currently academician of Chinese Academy of Sciences and research professor of Innovation Academy for Precision Measurement Science and Technology, Chinese Academy of Sciences. His current research interests include the signal detection, theoretical simulation and mechanism study of high-precision gravity variations induced by Earth's micro deformation and geodynamics.